

Electrode and electroactive polymer layout design using topology optimization

Daniel Hård^{1,*}, Mathias Wallin¹, and Matti Ristinmaa¹

¹Division of Solid Mechanics, Lund University, Box 118, SE-22100 Lund, Sweden

*Corresponding author: Daniel Hård, daniel.hard@solid.lth.se

Abstract

When electrically stimulated, electroactive polymers (EAPs) respond with mechanical deformation. The goal of this work is to design electrode and EAP layouts simultaneously in structures by using density-based, multi-material topology optimization. In this novel approach the layout of electrodes and EAP material are not given a priori but is a result from the topology optimization. Material interpolation based on exponential functions is introduced, allowing a large flexibility to control the material interpolation. The electric field in the surrounding free space is modeled using a truncated extended domain method. Numerical examples that demonstrates the method's ability to design arbitrary EAP and electrode layouts are presented. In these optimized structures, electrode material is continuously connected from the electrical sources to opposite sides of the EAP material and thereby concentrating the electric field to the EAP material which drives the deformation.

Keywords: Multi-material, Topology optimization, Electroactive polymer, Electrode, Free space

1 Introduction

Electro-mechanically coupled materials deform when electrically stimulated. One example is piezoelectric materials where electric field and deformation are linearly coupled. Another example is electroactive polymers (EAPs) which has a non-linear coupling. Dielectric EAPs, which is the subject of this study, is an active research area which has great potential in, e.g., artificial muscles and actuators

[1, 2]. Typically, dielectric EAPs are constructed as thin layer of EAP material sandwiched between two compliant electrodes such that a potential difference will cause the EAP to contract in the direction of the electric field.

Modeling and design of EAPs has attracted much attention, see, e.g., Dorfmann and Ogden [3], Ask et al. [4, 5, 6], Ortigosa and Gil [7]. In recent years, there has been a growing interest into combining EAPs and topology optimization. Bortot et al. [8] used topology optimization with a genetic algorithm to design dielectric elastomer structures with tunable band gaps. This problem was later solved more efficiently using gradient-based optimization by Sharma et al. [9]. Ortigosa et al. [10] used topology optimization to optimize the active EAP layer. This was developed into a multi-resolution model by Ortigosa and Martínez-Frutos [11]. In Martínez-Frutos et al. [12] the electrode placement was optimized, however they only considered the electrodes as a 2D-layer of nodes, not as a separate material. Recently, electrode connectivity was investigated by Hård et al. [13], where the shape of the electrodes were implicitly given by the solid material phase.

The goal in this work is to develop a topology optimization methodology capable of generating arbitrary EAP and electrode layouts. With this approach, the layout of electrode and EAP material is not given a priori but is an outcome of the topology optimization. This requires the use of multi-material topology optimization.

Multi-material topology optimization can be used to find the optimal distribution of multiple different material phases. The commonly used SIMP method, see Bendsoe and Sigmund [14], can be extended to handle multiple materials. Alternative methods include, e.g., Discrete Material Optimization (DMO) by Stegmann and Lund [15] and Unified Material Interpolation (UMI) by Yi et al. [16]. In the context of multi-material optimization of coupled problems, Granlund et al. [17] considered transient thermo-mechanical problems and He et al. [18] considered piezoelectric structures for energy harvesting. Hu et al. [19] investigated multi-material and multi-scale topology optimization of structures with embedded piezoelectric actuators. Almeida et al. [20] proposed a method for simultaneous optimization of dielectric and conductive materials together with a geometry projection method for embedded piezoelectric stack actuators. Ortigosa et al. [21] investigated multi-material shape morphing of layered EAPs, but did not optimize the electrodes explicitly.

In most research on EAPs, only solid bodies were modeled. This is a reasonable approach for materials with large permittivity, e.g., piezoelectric materials. In the present case of dielectric EAPs, the permittivity is significantly smaller and approximately of the same or one order larger than vacuum. This will have substantial influence on the modeling of the EAP. Multiple approaches to model the electric fields in the surrounding free space for electrostatic conditions exist, see,

e.g., Chen and Konrad [22]. Vu and Steinmann [23, 24] used a coupled BEM-FEM method to model the electric field in the space surrounding an EAP. Pelteret et al. [25] used a truncated free space in the study of a mixed variational formulation for quasi-incompressible electroactive and magnetoactive polymers. Dev et al. [26] incorporated a truncated free space in the context of topology optimization and this methodology is adapted in the current work.

The structure of this paper is as follows. In Section 2 the EAP model is described. In Section 3, the topology optimization formulation is developed. Numerical examples that demonstrates the method's ability to generate arbitrary EAP and electrode layouts are shown in Section 4. Lastly, Section 5 provides conclusions.

2 Non-linear electro-elasticity with free space

In this section, the governing non-linear electro-elastic balance laws restricted to electrostatic condition will be introduced. For a detailed presentation of the topic, the reader is referred to Jackson [27], Eringen and Maugin [28], Kovetz [29], and Dorfmann and Ogden [3]. Modeling the surrounding free space is especially important for the electric field, since it is not restricted to the solid body. This work models the free space as a truncated extended domain presented in Dev et al. [26], where the free space is modeled as a very soft elastic material with vacuum permittivity properties.

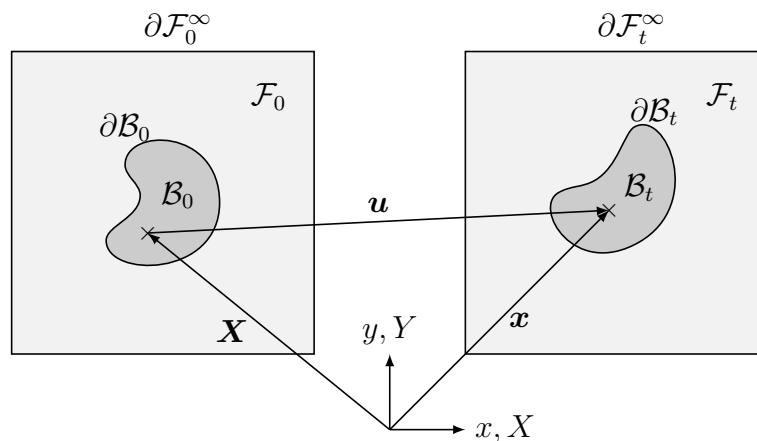


Figure 1: A solid body \mathcal{B}_0 surrounded by a free space \mathcal{F}_0 in the material and spatial configurations.

Fig. 1 illustrates the considered domain in both the material and spatial configurations. The domain consists in the material configuration of a body \mathcal{B}_0 and the surrounding free space \mathcal{F}_0 such that the undeformed domain is given by $\mathcal{B}_0 \cup \mathcal{F}_0$

and $\mathcal{B}_0 \cap \mathcal{F}_0 = \emptyset$. When deformed, \mathcal{B}_0 and \mathcal{F}_0 are mapped to \mathcal{B}_t and \mathcal{F}_t , respectively. Particles are labeled by their coordinates $\mathbf{X} \in \mathcal{B}_0 \cup \mathcal{F}_0$ and their placement $\mathbf{x} \in \mathcal{B}_t \cup \mathcal{F}_t$ is described by the smooth mapping $\mathbf{x}(\mathbf{X}) = \boldsymbol{\varphi}(\mathbf{X})$. The deformation is locally described by the deformation gradient $\mathbf{F} = \nabla_{\mathbf{X}} \boldsymbol{\varphi}$ and the local volume change $J = \det(\mathbf{F})$. The hyper-elastic material response will be governed by the right Cauchy-Green tensor defined as $\mathbf{C} = \mathbf{F}^T \cdot \mathbf{F}$ and its isochoric part $\overline{\mathbf{C}} = J^{-2/3} \mathbf{C}$.

2.1 Balance relations

Assuming quasi-electrostatics, the Maxwell-Faraday equation becomes $\nabla_{\mathbf{X}} \times \mathbf{E} = \mathbf{0}$, implying that the electric field \mathbf{E} is obtained from the gradient of a continuous scalar electric potential ϕ as $\mathbf{E} = -\nabla_{\mathbf{X}} \phi$, where the negative sign is introduced by convention.

Gauss's law, assuming no free volume charge density in the dielectric material, is formulated as

$$\nabla_{\mathbf{X}} \cdot \mathbf{D} = 0, \quad \text{in } \mathcal{F}_0 \cup \mathcal{B}_0, \quad (1a)$$

$$\phi = \phi_g, \quad \text{on } \partial \mathcal{B}_0^{g,\phi}, \quad (1b)$$

$$\mathbf{D} \cdot \mathbf{N} = 0, \quad \text{on } \partial \mathcal{F}_0^\infty, \quad (1c)$$

$$-[[\mathbf{D}]] \cdot \mathbf{N} = D_N, \quad \text{on } \partial \mathcal{B}_0^{h,\phi}, \quad (1d)$$

where \mathbf{D} is the electric displacement. The boundary $\partial \mathcal{B}_0$ to \mathcal{B}_0 is split such that $\partial \mathcal{B}_0 = \partial \mathcal{B}_0^{h,\phi} \cup \partial \mathcal{B}_0^{g,\phi}$ and $\partial \mathcal{B}_0^{h,\phi} \cap \partial \mathcal{B}_0^{g,\phi} = \emptyset$. The boundary condition (1b) represents the prescribed electric potential on the boundary part $\partial \mathcal{B}_0^{g,\phi}$, and the boundary condition (1d) represents the prescribed free surface charge density on the boundary part $\partial \mathcal{B}_0^{h,\phi}$, with the outward unit normal \mathbf{N} to the body \mathcal{B}_0 . The jump $[[\bullet]] = [\bullet]^+ - [\bullet]^-$ is the difference in the value (\bullet) between inside and outside the body. The condition in (1c) on the far-field boundary $\partial \mathcal{F}_0^\infty$ ensures that the electric field becomes zero at large distances from the solid body.

In the absence of body forces, the balance of linear momentum for quasi-static electro-mechanics is provided by

$$\nabla_{\mathbf{X}} \cdot \mathbf{T} = \mathbf{0}, \quad \text{in } \mathcal{F}_0 \cup \mathcal{B}_0, \quad (2a)$$

$$\varphi = \varphi_g, \quad \text{on } \partial \mathcal{B}_0^{g,\varphi}, \quad (2b)$$

$$\varphi = \mathbf{0}, \quad \text{on } \partial \mathcal{F}_0^\infty, \quad (2c)$$

$$[[\mathbf{T}]] \cdot \mathbf{N} = \mathbf{T}_N, \quad \text{on } \partial \mathcal{B}_0^{h,\varphi}, \quad (2d)$$

where \mathbf{T} is the total first Piola-type stress tensor. The boundary $\partial \mathcal{B}_0$ to \mathcal{B}_0 is split such that $\partial \mathcal{B}_0 = \partial \mathcal{B}_0^{h,\varphi} \cup \partial \mathcal{B}_0^{g,\varphi}$ and $\partial \mathcal{B}_0^{h,\varphi} \cap \partial \mathcal{B}_0^{g,\varphi} = \emptyset$. The boundary condition

in (2b) represents the prescribed displacement on $\partial\mathcal{B}_0^{g,\varphi}$, (2c) represents the fixed displacement at large distances, and (2d) represents the prescribed total traction on $\partial\mathcal{B}_0^{h,\varphi}$. It is assumed that the free space can be modeled with (2a).

2.2 Constitutive model

The constitutive dielectric EAP model used in this work can be found in, e.g., Ask et al. [4, 5, 6], in this work the viscoelasticity contribution is omitted. For simplicity, the same model is used to model the electrode material. An augmented free energy function $\Omega(\mathbf{F}, \mathbf{E})$ can be introduced, see, e.g., Dorfmann and Ogden [3], which defines \mathbf{D} and \mathbf{T} , i.e.,

$$\mathbf{D}(\mathbf{F}, \mathbf{E}) = -\frac{\partial\Omega(\mathbf{F}, \mathbf{E})}{\partial\mathbf{E}}, \quad \mathbf{T}(\mathbf{F}, \mathbf{E}) = \frac{\partial\Omega(\mathbf{F}, \mathbf{E})}{\partial\mathbf{F}}, \quad (3)$$

where the augmented free energy function is taken as

$$\begin{aligned} \Omega(\mathbf{F}, \mathbf{E}) = & \frac{1}{2}K(J-1)^2 + \frac{1}{2}G(\overline{\mathbf{C}} : \mathbf{I} - 3) \\ & - \frac{1}{2}\varepsilon_0\varepsilon_r J \mathbf{E} \cdot \mathbf{C}^{-1} \cdot \mathbf{E} + c_e \mathbf{E} \cdot \mathbf{E}, \end{aligned} \quad (4)$$

where K and G are the bulk and shear modulus, respectively, $\varepsilon_0 \approx 8.854 \cdot 10^{-12} \text{ F m}^{-1}$ the vacuum permittivity, ε_r is the relative permittivity, and c_e an electrical material constant.

Inserting (4) in (3) yields

$$\mathbf{D}(\mathbf{F}, \mathbf{E}) = \varepsilon_0\varepsilon_r J \mathbf{E} \cdot \mathbf{C}^{-1} - 2c_e \mathbf{E}, \quad (5)$$

and

$$\begin{aligned} \mathbf{T}(\mathbf{F}, \mathbf{E}) = & K(J-1)J\mathbf{F}^{-T} + GJ^{-2/3} \left[\mathbf{F} - \frac{1}{3}[\mathbf{C} : \mathbf{I}]\mathbf{F}^{-T} \right] \\ & + \varepsilon_0\varepsilon_r J \left[(\mathbf{E} \cdot \mathbf{F}^{-1}) \otimes (\mathbf{E} \cdot \mathbf{C}^{-1}) - \frac{1}{2}(\mathbf{E} \cdot \mathbf{C}^{-1} \cdot \mathbf{E})\mathbf{F}^{-T} \right]. \end{aligned} \quad (6)$$

The free space is modeled as void material in the topology optimization introduced in Section 3. It is well known that the Neo-Hookean approach in (4) can introduce instabilities, which could be resolved with a linear elasticity model, e.g. by gamma scaling as in Wang et al. [30]. This was however not necessary in this work. Additional problems noted in Ortigosa et al. [10] is that the electro-mechanical term in (4) may result in numerical instabilities due to high non-convexity. Therefore, the stabilized formulation proposed by Ortigosa et al. [10] is used instead, which removes the dependency on the deformation gradient.

The same approach was also used in Dev et al. [26]. The free energy for the void region is taken as

$$\begin{aligned}\Omega^{\text{void}}(\mathbf{F}, \mathbf{E}) &= \frac{1}{2} K^{\text{void}} (J - 1)^2 + \frac{1}{2} G^{\text{void}} (\overline{\mathbf{C}} : \mathbf{I} - 3) \\ &\quad - \frac{1}{2} \varepsilon_0 \mathbf{E} \cdot \mathbf{E},\end{aligned}\tag{7}$$

where K^{void} and G^{void} are sufficiently small modeling parameters to not significantly influence the mechanical response while large enough to avoid numerical convergence issues.

2.3 Variational forms and finite element discretization

The weak forms of Gauss's law (1a) and the electro-mechanical balance of linear momentum (2a) in the material configuration including both the body \mathcal{B}_0 and the free space \mathcal{F}_0 are

$$\delta W^{\text{elt}} = \delta W_{\text{ext}}^{\text{elt}} - \delta W_{\text{int}}^{\text{elt}} = 0, \quad \forall \delta \phi \in [v|v = 0 \text{ on } \partial \mathcal{B}_0^{g,\phi}],\tag{8a}$$

$$\delta W^{\text{mec}} = \delta W_{\text{ext}}^{\text{mec}} - \delta W_{\text{int}}^{\text{mec}} = 0, \quad \forall \delta \boldsymbol{\varphi} \in [v|\mathbf{v} = \mathbf{0} \text{ on } \partial \mathcal{B}_0^{g,\varphi} \cup \partial \mathcal{F}_0^\infty],\tag{8b}$$

where

$$\delta W_{\text{ext}}^{\text{elt}} = - \int_{\partial \mathcal{B}_0^{h,\phi}} \delta \phi D_N dA,\tag{9a}$$

$$\delta W_{\text{int}}^{\text{elt}} = \int_{\mathcal{F}_0 \cup \mathcal{B}_0} \nabla_X \delta \phi \cdot \mathbf{D} dV,\tag{9b}$$

$$\delta W_{\text{ext}}^{\text{mec}} = \int_{\partial \mathcal{B}_0^{h,\varphi}} \delta \boldsymbol{\varphi} \cdot \mathbf{T}_N dA,\tag{9c}$$

$$\delta W_{\text{int}}^{\text{mec}} = \int_{\mathcal{F}_0 \cup \mathcal{B}_0} \nabla_X \delta \boldsymbol{\varphi} : \mathbf{T} dV.\tag{9d}$$

A standard nonlinear finite element formulation is used to discretize (8a) and (8b) where the same shape functions are used to interpolate both the displacements $\boldsymbol{\varphi}$ and potential ϕ as $\boldsymbol{\varphi} \approx \mathbf{N}^\varphi \mathbf{a}^\varphi$ and $\phi \approx \mathbf{N}^\phi \mathbf{a}^\phi$, where \mathbf{a}^φ and \mathbf{a}^ϕ are the nodal values and \mathbf{N}^φ and \mathbf{N}^ϕ the corresponding global shape functions. Only one additional degree of freedom is needed for the potential. The virtual displacements and virtual electric potential are approximated using the Galerkin approach as $\delta \boldsymbol{\varphi} \approx \mathbf{N}^\varphi \delta \mathbf{a}^\varphi$ and $\delta \phi \approx \mathbf{N}^\phi \delta \mathbf{a}^\phi$, where $\delta \mathbf{a}^\varphi$ and $\delta \mathbf{a}^\phi$ are the virtual nodal values.

The finite element approximations inserted into (8a) and (8b) together with the arbitrariness of $\delta \mathbf{a}^\varphi$ and $\delta \mathbf{a}^\phi$ results in the residual equations on matrix format

$$\mathbf{r}^\phi = \mathbf{f}_{ext}^\phi - \mathbf{f}_{int}^\phi = \mathbf{0}, \quad (10a)$$

$$\mathbf{r}^\varphi = \mathbf{f}_{ext}^\varphi - \mathbf{f}_{int}^\varphi = \mathbf{0}, \quad (10b)$$

where

$$\mathbf{f}_{ext}^\phi = \int_{\partial\mathcal{B}_0^{h,\phi}} \mathbf{N}^{\phi,T} D_N dA, \quad (11a)$$

$$\mathbf{f}_{int}^\phi = \int_{\mathcal{F}_0 \cup \mathcal{B}_0} \mathbf{B}^{\phi,T} \mathbf{D} dV, \quad (11b)$$

$$\mathbf{f}_{ext}^\varphi = \int_{\partial\mathcal{B}_0^{h,\varphi}} \mathbf{N}^{\varphi,T} \mathbf{T}_N dA, \quad (11c)$$

$$\mathbf{f}_{int}^\varphi = \int_{\mathcal{F}_0 \cup \mathcal{B}_0} \mathbf{B}^{\varphi,T} \mathbf{T} dV, \quad (11d)$$

where \mathbf{B}^ϕ and \mathbf{B}^φ contains the gradients of \mathbf{N}^ϕ and \mathbf{N}^φ .

Newton's method is used to solve (10a) and (10b). Linearization and assuming dead loading condition yields a discretized and linearized system, which in monolithic matrix format it is formulated as

$$\mathbf{K} \Delta \mathbf{a} = \begin{bmatrix} \mathbf{K}^{\varphi\varphi} & \mathbf{K}^{\phi\varphi} \\ \mathbf{K}^{\phi\varphi} & \mathbf{K}^{\phi\phi} \end{bmatrix} \begin{bmatrix} \Delta \mathbf{a}^\varphi \\ \Delta \mathbf{a}^\phi \end{bmatrix} = \begin{bmatrix} \mathbf{r}^\varphi \\ \mathbf{r}^\phi \end{bmatrix} = \mathbf{r}, \quad (12)$$

which provides the Newton updates

$$\mathbf{a}^\varphi \leftarrow \mathbf{a}^\varphi + \Delta \mathbf{a}^\varphi, \quad \mathbf{a}^\phi \leftarrow \mathbf{a}^\phi + \Delta \mathbf{a}^\phi, \quad (13)$$

and continues until the residuals in (10a) and (10b) are sufficiently small.

The partitions of \mathbf{K} in (12) are obtained from linearizations of (11b) and (11d), i.e.,

$$\begin{aligned} \mathbf{K}^{\phi\phi} &= \int_{\mathcal{F}_0 \cup \mathcal{B}_0} \mathbf{B}^{\phi,T} \mathbf{D}^{\text{elt}} \mathbf{B}^\phi dV, \\ \mathbf{K}^{\varphi\phi^T} = \mathbf{K}^{\phi\varphi} &= - \int_{\mathcal{F}_0 \cup \mathcal{B}_0} \mathbf{B}^{\phi,T} \mathbf{D}^{\text{mix}} \mathbf{B}^\varphi dV, \\ \mathbf{K}^{\varphi\varphi} &= \int_{\mathcal{F}_0 \cup \mathcal{B}_0} \mathbf{B}^{\varphi,T} \mathbf{D}^{\text{mec}} \mathbf{B}^\varphi dV, \end{aligned} \quad (14)$$

where \mathbf{D}^{elt} , \mathbf{D}^{mix} and \mathbf{D}^{mec} are the Voigt representation of the material tangents,

$$\mathbf{D}^{\text{elt}} = \frac{\partial^2 \Omega}{\partial \mathbf{E} \otimes \partial \mathbf{E}}, \quad \mathbf{D}^{\text{mix}} = \frac{\partial^2 \Omega}{\partial \mathbf{E} \otimes \partial \mathbf{F}}, \quad \mathbf{D}^{\text{mec}} = \frac{\partial^2 \Omega}{\partial \mathbf{F} \otimes \partial \mathbf{F}}, \quad (15)$$

where \mathbf{D}^{elt} is second order, \mathbf{D}^{mix} third order, and \mathbf{D}^{mec} fourth order tensors.

3 Topology optimization

The design, in the undeformed body domain \mathcal{B}_0 , is defined by the two piecewise uniform density fields ρ_1 and ρ_2 . Each finite element e in \mathcal{B}_0 is associated with two uniform element densities $\rho_i^e \in [0,1]$ which are collected in the design vectors $\boldsymbol{\rho}_1$ and $\boldsymbol{\rho}_2$. The density field ρ_1 controls the amount of solid material and ρ_2 if the solid material is electrode or EAP. This is further explained in Section 3.2.

Using a nested format, the general form of the optimization problem is formulated as

$$(\text{TO}) \begin{cases} \min_{\boldsymbol{\rho}_1, \boldsymbol{\rho}_2} g_0 \\ \text{subjected to } \begin{cases} g_j \leq 0, & j = 1, \dots, n_{constr} \\ 0 \leq \rho_i^e \leq 1, & \forall e \in [1, \dots, n_{elm}], i \in [1, 2] \end{cases} \end{cases} \quad (16)$$

The objective is to maximize the displacements, i.e.,

$$g_0(\mathbf{a}) = \mathbf{l}^T \mathbf{a}, \quad (17)$$

where \mathbf{l} is a constant vector with nonzero entries in the dofs which should be maximized, \mathbf{a} is the solution vector at the terminal load step.

To limit the volume of each material phase, volume constraints are enforced in (16) as,

$$g_1 = \frac{V_1}{\alpha_1 V_{DD}} - 1 \leq 0, \quad g_2 = \frac{V_2}{\alpha_2 V_{DD}} - 1 \leq 0, \quad (18)$$

where α_1 and α_2 are the allowed volume fractions and $V_{DD} = \text{vol}(\mathcal{B}_0)$ is the volume of the design domain. In (18), the volumes V_1 and V_2 of phase 1 and phase 2 are computed as

$$V_1 = \int_{\mathcal{B}_0} \bar{\rho}_1 (1 - \bar{\rho}_2) \, dV, \quad V_2 = \int_{\mathcal{B}_0} \bar{\rho}_1 \bar{\rho}_2 \, dV, \quad (19)$$

where $\bar{\rho}_1$ and $\bar{\rho}_2$ are the filtered and thresholded densities as presented in Section 3.1.

3.1 Regularization, projection, and intermediate densities

The piecewise uniform density fields ρ_1 and ρ_2 are regularized by smoothing using the partial differential equation (PDE) filter proposed by Lazarov and Sigmund [31],

$$-l_i^2 \Delta_{\mathbf{X}} \tilde{\rho}_i + \tilde{\rho}_i = \rho_i, \quad \text{in } \mathcal{B}_0, \quad (20a)$$

$$\nabla_{\mathbf{X}} \tilde{\rho}_i \cdot \mathbf{N} = 0, \quad \text{on } \partial \mathcal{B}_0, \quad (20b)$$

where $\Delta_{\mathbf{x}}$ is the material Laplacian operator, $l_i > 0$ is the filter length scale parameter, and $\tilde{\rho}_i$ the filtered, continuous fields. Note the possibility to use different length scales for $\tilde{\rho}_1$ and $\tilde{\rho}_2$. The boundary condition in (20b) tends to generate designs that artificially place material at the boundaries of \mathcal{B}_0 . To reduce this, Wallin et al. [32] proposed using a Robin boundary condition, however this was not further investigated in this work.

Utilizing the same discretization as in the state problem render a linear system on the form,

$$\mathbf{A}\tilde{\rho}_i = \mathbf{G}\rho_i, \quad (21)$$

where the matrices \mathbf{A} and \mathbf{G} are design independent and only assembled once.

The amount of intermediate densities caused by the filter in (20a) is decreased by the smooth Heaviside projection introduced by Wang et al. [33] as,

$$\bar{\rho}_i = H_{\beta,\eta}(\tilde{\rho}_i) = \frac{\tanh(\beta\eta) + \tanh(\beta(\tilde{\rho}_i - \eta))}{\tanh(\beta\eta) + \tanh(\beta(1 - \eta))}, \quad (22)$$

where β controls the sharpness and η the projection threshold. The projection (22) was applied on the filtered density fields $\tilde{\rho}_i$ in every Gauss point separately for the two density fields.

Despite the Heaviside projection in (22), the optimization might still generate designs with intermediate densities. To penalize intermediate densities, the penalization proposed in Thillaithevan et al. [34] and Granlund and Wallin [35], is adopted as,

$$\bar{g}_0 = g_0 + a_d \sum_{i=1}^2 d_\delta^\alpha(\bar{\rho}_i), \quad (23)$$

where a_d is a scale factor and

$$d_\delta^\alpha(\bar{\rho}_i) = \frac{1}{V_{DD}} \int_{\mathcal{B}_0} 4^\alpha (\bar{\rho}_i + \delta)^\alpha (1 - \bar{\rho}_i + \delta)^\alpha dV, \quad (24)$$

where V_{DD} normalizes the expression. In (24), $0 < \alpha \leq 1$ and $0 < \delta \ll 1$ are needed to avoid singularities at $\bar{\rho}_i = 0$ and $\bar{\rho}_i = 1$ in the sensitivities. Examples of the penalization are given in Fig. 2.

3.2 Material interpolation

The commonly used SIMP material interpolation, see Bendsøe and Sigmund [14], results in that the highest sensitivities always occur for $\bar{\rho} = 1$, regardless of interpolation order. Other methods for multi-material interpolation include DMO, see Stegmann and Lund [15], and UMI, see Yi et al. [16]. Both of these methods have the advantage that they are independent of interpolation order. However,

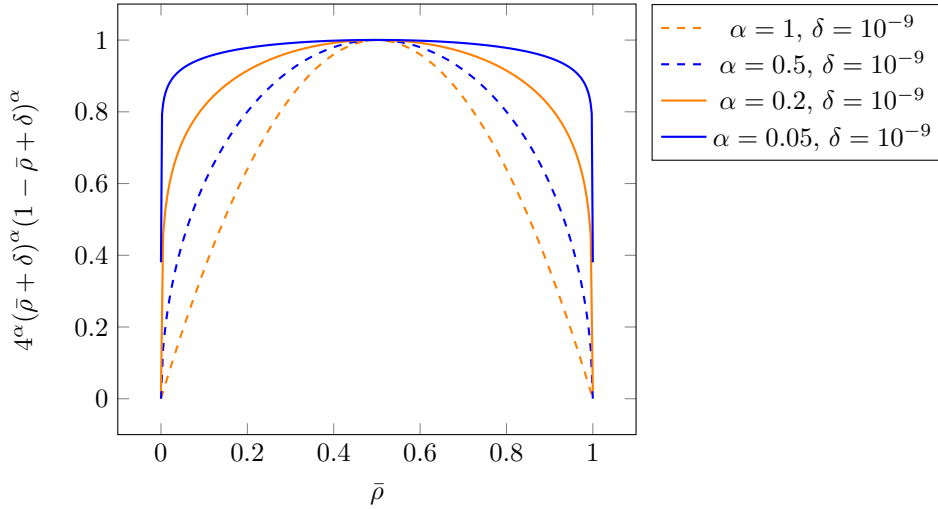


Figure 2: The penalization function in (24) with example values on α and δ .

numerical tests showed that in the current application, especially in combination with the penalization in (24), these methods were not able to generate distinct material phases.

To remedy these problems, a formulation based on exponential functions is proposed in this work denoted as Exponential Material Interpolation (EMI),

$$\chi_q(\bar{\rho}) = \frac{e^{q\bar{\rho}} - 1}{e^q - 1}, \quad (25)$$

where q is a penalization parameter. A similar function was proposed in Ye et al. [36] as a filter function, denoted composite exponential function (CEF).

To exemplify the EMI and the influence of the penalization parameter q , consider the interpolation between two materials

$$\xi = \xi^1 + \chi_q(\bar{\rho})(-\xi^1 + \xi^2), \quad (26)$$

which is shown in Fig. 3. The sign of the parameter q determines if the highest sensitivities are at $\bar{\rho} = 0$ or $\bar{\rho} = 1$. The interpolation is also symmetric around $\bar{\rho} = 0.5$ when switching the order of the phases and the sign of q .

The three phase multi-material interpolation can now be formulated as

$$\xi = \xi^0 + \chi_{q_1^\xi}(\bar{\rho}_1)(-\xi^0 + \xi^1 + \chi_{q_2^\xi}(\bar{\rho}_2)(-\xi^1 + \xi^2)), \quad (27)$$

where ξ^i represents the material parameters K , G , ε_r and c_e , in the void material and the two solid materials, electrode and EAP. In this interpolation scheme, $\bar{\rho}_1 = 0$ models void and $\bar{\rho}_1 = 1$ solid material. Similarly for the solid material, where $\bar{\rho}_2 = 0$ models electrode and $\bar{\rho}_2 = 1$ models EAP. Due to the symmetry properties of EMI, the interpolation is independent of the order of the two solid materials.

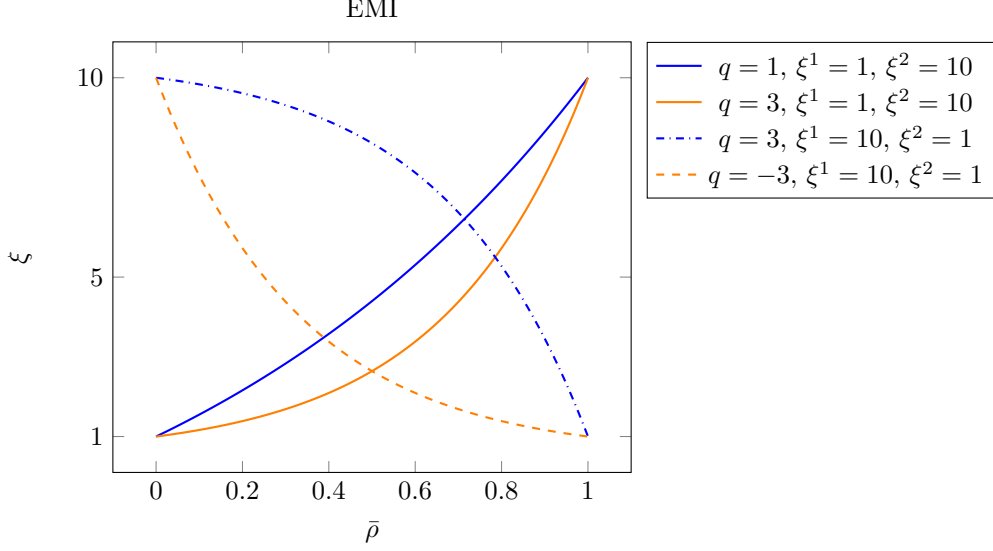


Figure 3: The EMI interpolation in (26) with example values on ξ^1 , ξ^2 , and q .

3.3 Sensitivity analysis

The design updates are obtained using the gradient based MMA, see Svanberg [37], which uses gradients of the objective and constraint functions g_j w.r.t. each of the design variables ρ_i . Because regularization is performed via the PDE filter in (20a) and (20b), the chain rule is applied to the objective and constraint functions such that

$$\frac{\partial g_j}{\partial \rho_i} = \frac{\partial g_j}{\partial \tilde{\rho}_i} \frac{\partial \tilde{\rho}_i}{\partial \rho_i}, \quad (28)$$

where $\frac{\partial \tilde{\rho}_i}{\partial \rho_i}$ is obtained from the discretized form of the filter in (21).

The sensitivity of the objective function for maximizing displacements in (17) is calculated with the adjoint method wherein the original objective function g_0 is augmented by an adjoint vector $\boldsymbol{\mu}$ multiplied by the coupled residual in (12),

$$\tilde{g}_0(\mathbf{a}, \tilde{\boldsymbol{\rho}}) = g_0 - \boldsymbol{\mu}^T \mathbf{r}. \quad (29)$$

The sensitivities w.r.t. the filtered densities $\tilde{\rho}_i$ is thus computed as

$$\frac{\partial \tilde{g}_0(\mathbf{a}, \tilde{\boldsymbol{\rho}})}{\partial \tilde{\rho}_i} = \frac{\partial \tilde{g}_0}{\partial \tilde{\rho}_i} + \frac{\partial \tilde{g}_0}{\partial \mathbf{a}} \frac{\partial \mathbf{a}}{\partial \tilde{\rho}_i} = -\boldsymbol{\mu}^T \frac{\partial \mathbf{r}}{\partial \tilde{\rho}_i} + (\mathbf{l}^T - \boldsymbol{\mu}^T \mathbf{K}) \frac{\partial \mathbf{a}}{\partial \tilde{\rho}_i}, \quad (30)$$

where the implicit sensitivity $\frac{\partial \mathbf{a}}{\partial \tilde{\rho}_i}$ is annihilated by assigning $\boldsymbol{\mu}$ to fulfill

$$\mathbf{K} \boldsymbol{\mu} = \mathbf{l}, \quad (31)$$

where \mathbf{K} is the coupled stiffness matrix in (12). Homogeneous Dirichlet boundary condition is enforced in all prescribed displacements and potential dofs.

Once (31) is solved for $\boldsymbol{\mu}$, the sensitivity reduces to

$$\frac{\partial \tilde{g}_0(\mathbf{a}, \tilde{\boldsymbol{\rho}})}{\partial \tilde{\rho}_i} = -\boldsymbol{\mu}^T \frac{\partial \mathbf{r}}{\partial \tilde{\rho}_i}. \quad (32)$$

4 Numerical examples

The parameters for the material phases are given in Tab. 1. The EAP material is modeled with electro-mechanical coupling while the electrode material is uncoupled. To mimic the electrical conductivity of the electrode, a very large value of the c_e parameter in (4) is used, while a low value is used for the EAP material. Vacuum permittivity is assumed for the void material and without any electro-mechanical coupling. The electrode is stiffer than EAP and the void stiffness is sufficiently small to not have a significant mechanical influence while avoiding numerical convergence issues. Additional assumptions are that $D_N = 0$ in (1d) and $\mathbf{T}_N = \mathbf{0}$ in (2d).

Table 1: Material parameters for the different phases

| Material | K [MPa] | G [MPa] | c_e [N V ⁻²] | ε_r [-] |
|-----------|---------------------|---------------------|--|---------------------|
| EAP | 0.6 | 0.1 | $-\frac{1}{2}\varepsilon_0$ | 4.7 |
| Electrode | $0.6 \cdot 10$ | $0.1 \cdot 10$ | $-\frac{1}{2}\varepsilon_0 \cdot 10^5$ | 0 |
| Void | $0.6 \cdot 10^{-9}$ | $0.1 \cdot 10^{-9}$ | $-\frac{1}{2}\varepsilon_0$ | 0 |

To reduce the computational cost, the free space discretization is coarser than the solid body and graded with larger elements at large distances from the optimized structure. Algorithm 1 presents a pseudo-code for implementation.

An actuator suspended in a free space, as illustrated in Fig. 4, is activated by a prescribed positive and negative potential in the upper and lower left edges respectively, where $\phi_p = 3$ kV, i.e., the external source is connected to these two electrode locations. It is assumed that the two electrode locations are fixed in space, i.e., clamped. The two objective functions investigated in this example are vertical and horizontal output displacements, u_{out}^v and u_{out}^h , respectively, also illustrated in Fig. 4. Two springs with spring stiffness $k_s^v = k_s^h = 10^{-3}dG^{\text{EAP}}$ are connected to the corresponding output ports to simulate the stiffness of the actuated object and with the thickness $d = 1$ mm. The vector \mathbf{l} in (17) is defined such that only the displacement u_{out}^v or u_{out}^h on the right port indicated in Fig. 4 are extracted from \mathbf{a} .

Algorithm 1 Optimization algorithm

Set initial values on all parameters
 Set ρ_i for the initial design
while $|g_0^k - g_0^{k-1}| > TOL|g_0^k|$ **do**
 Update relevant parameters
 Apply filter (21) to obtain $\tilde{\rho}_i$ from ρ_i
 Apply threshold (22) to obtain $\bar{\rho}_i$ from $\tilde{\rho}_i$
 Solve state problem (10a) and (10b) using (12)
 Calculate objective and constraints $g_j, j = 0, 1, \dots, n_{constr}$
 Compute sensitivities using the adjoint method
 Update element design variables ρ_i using MMA
end while

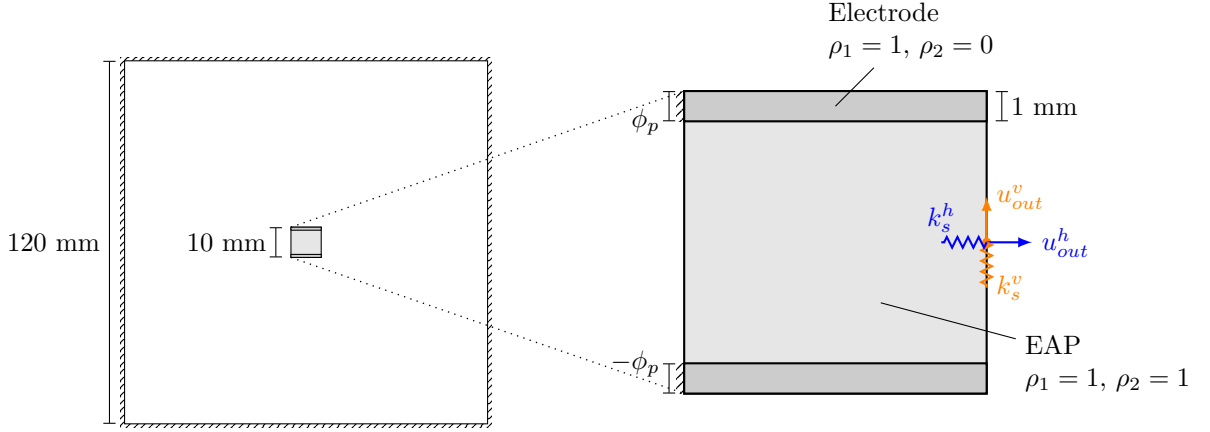


Figure 4: Illustration of the geometry and boundary conditions for the actuator with thickness 1 mm. The square design domain is surrounded by a large free space. The initial design and the two cases for the optimization are presented.

The initial design in Fig. 4 consists of electrode and EAP material indicated with darker and lighter gray, respectively. The initial density values are $\rho_1 = 1$ everywhere and $\rho_2 = 0$ for the electrode material and $\rho_2 = 1$ for the EAP material.

The design domain \mathcal{B}_0 is discretized using $200 \times 200 \times 1 = 40\,000$ 8-node brick elements while the free space \mathcal{F}_0 is resolved using an 11 285 element graded mesh. Plane strain is enforced by constraining the displacement in the out-of-plane direction. Although 2D elements could be used, a 3D framework is used as this allows for a smooth transition to 3D in future works.

The filter parameter in (20a) is $l_i = 0.25$ mm. A continuation scheme is employed for the thresholding parameter β in (22), which is initiated to $\beta = 1$ and then increased by 20% every 10th iteration to a terminal value of 20. The parameter $\eta = 0.5$ is fixed.

Inspired by Ortigosa et al. [10], the electro-mechanical coupling terms are penalized more than the purely mechanical to ensure low electro-mechanical coupling in void and intermediate regions. The electrical terms has the same penalization as the electro-mechanical. A continuation scheme is utilized where the initial and final penalization parameters for EMI are given in Tab. 2 and the values is updated with 20% every 10th iteration until the final values are reached.

Table 2: Initial and final penalization parameters for EMI

| i | Initial | | | Final | | |
|-----|---------|-------------|------------|---------|-------------|------------|
| | q_i^m | q_i^{mel} | q_i^{el} | q_i^m | q_i^{mel} | q_i^{el} |
| 1 | 1 | 2 | 2 | 4 | 8 | 8 |
| 2 | -1 | 2 | -2 | -4 | 8 | -8 |

The output displacement varies with multiple orders of magnitude, therefore is g_0 is replaced by

$$\hat{g}_0 = a_1 \operatorname{asinh}(a_2 g_0), \quad (33)$$

where $a_1 = 10$ and $a_2 = 10^7$ to obtain a suitable MMA scaling. The allowed volume fractions are $\alpha_1 = 0.2$ and $\alpha_2 = 0.1$ and both constraint functions g_1 and g_2 are scaled by 10. Design updates continues until $|g_0^k - g_0^{k-1}| < TOL|g_0^k|$ during three consecutive iterations and all constraints were fulfilled, with the relative tolerance $TOL = 10^{-4}$.

A continuation scheme is employed for α and a_d in (23), while $\delta = 10^{-9}$ is constant. The penalization in (24) is initiated to $a_d = 0$ and after iteration 200 and until iteration 300, a_d is updated every 20th iteration such that $a_d = |\hat{g}_0|$. The parameter α is initiated as $\alpha = 0.9$ and after iteration 200 updated every 10th iteration with $\alpha = \max(\alpha - 0.1, 0.05)$.

The optimization formulation in (16) now becomes

$$(\text{TO})_1 \begin{cases} \min_{\rho_1, \rho_2} \bar{g}_0 = \hat{g}_0(g_0) + a_d \sum_{i=1}^2 d_\delta^\alpha(\bar{\rho}_i) \\ \text{subjected to} \begin{cases} g_j = \frac{V_j(\bar{\rho}_j)}{\alpha_j V_{DD}} - 1 \leq 0, & j = 1, 2 \\ 0 \leq \rho_i^e \leq 1, & \forall e \in [1, \dots, n_{elm}], i \in [1, 2] \end{cases} \end{cases} \quad (34)$$

Default MMA parameters is used with the exceptions for $\text{GHINIT} = 0.2$, $\text{GHINCR} = 1.1$, $\text{GMAXJ} = \text{XVAL}(J) - 0.0001 * \text{XMMJ}$ and $\text{HMINJ} = \text{XVAL}(J) + 0.0001 * \text{XMMJ}$.

Fig. 5a shows the optimized design $0.5 \leq \bar{\rho}_1$ when the vertical displacement is maximized. Electrode material is indicated with $\bar{\rho}_2 = 0$ and EAP with $\bar{\rho}_2 = 1$. Some electrode material is continuously connected from the electrical sources in the corners to opposite sides of the EAP material. Due to this, the electric potential

gradient, and thereby the electric field, is concentrated to within the EAP material, see Fig. 5b. This results in a thin active EAP layer which causes the deformation. Since the EAP material is curved with thicker electrode material on the upper side, it bends during activation. Traditional EAP structures are constructed in a similar fashion, where a thin layer of EAP material is sandwiched between electrodes.

From 5b, it is obvious that the highest electric fields occur within or close to the design domain. At the boundary $\partial\mathcal{F}_0^\infty$ the electric field is zero due to the boundary condition in (1c) and the potential approaches zero, which is expected.

Since the electrode material is stiffer than the EAP, it also stiffens the connection between the active layer and the output port. As the maximum amount of electrode material is utilized, see Fig. 5d, additional EAP material is used to stiffen the structure, but not activated.

Fig. 6a shows the optimized design when maximizing the horizontal displacement. Also in this case, the electrode material is continuously connected from the electrical sources in the corners to opposite sides of a thin EAP layer. The EAP layer stretches through the whole structure where the electric field is concentrated to three different parts, as can be seen in Fig. 6b. The generated deformations is thus transferred through the EAP layer to the output port, creating a horizontal dominated deformation.

The potentials in Figs. 6b and 5b are similar. The electrodes are shaped differently and much longer, which influences the free space potential, while still fulfilling the boundary condition on the far-field boundary.

Comparing Figs. 5c and 6c shows that the latter case requires more iterations to converge. During the first 200 iterations they behave similarly, but then the convergence is much slower when the horizontal displacement is optimized. The constraint functions in Figs. 5d and 6d behaves similarly, where the electrode material fulfills the volume fraction while the EAP volume constraint is inactive.

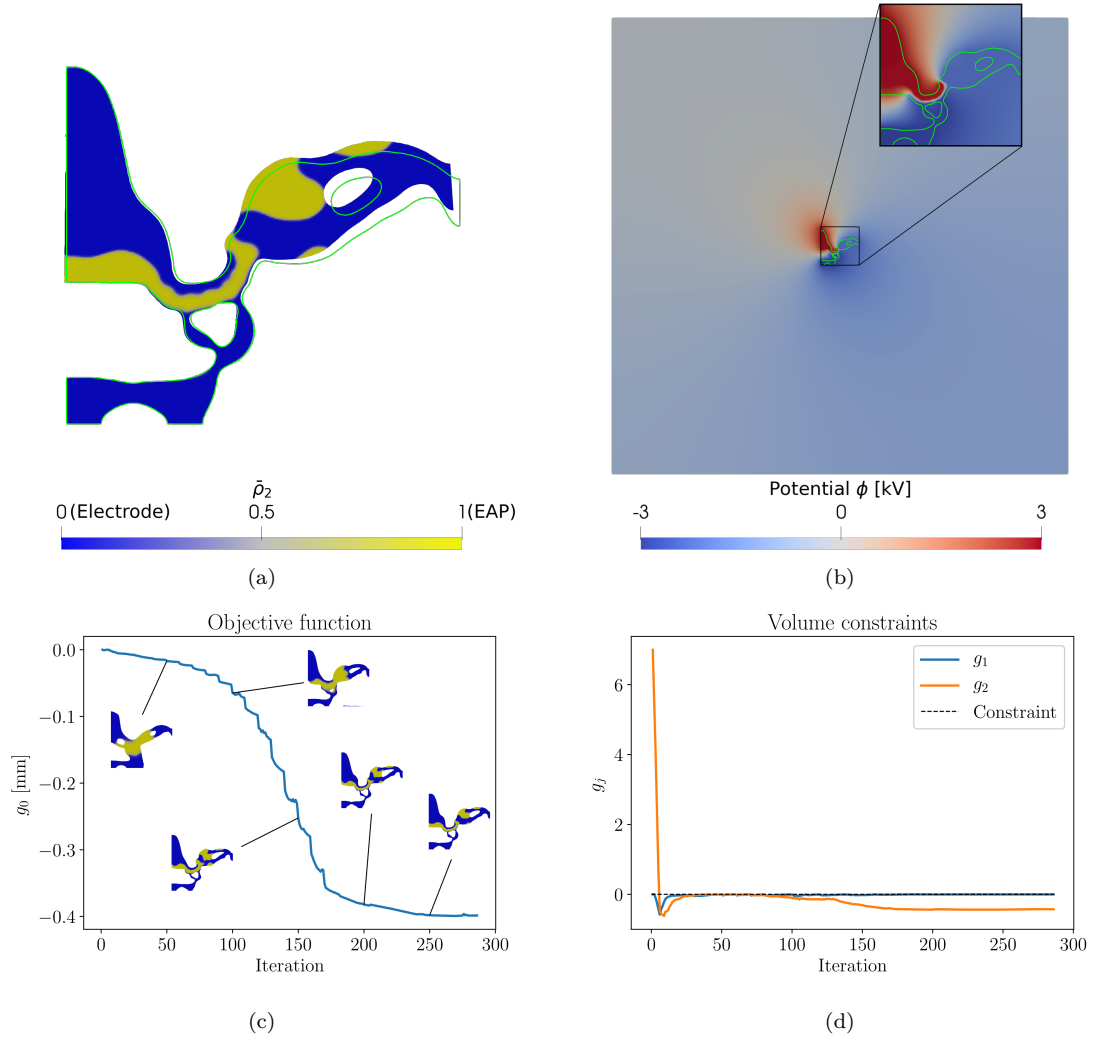


Figure 5: Optimized design for maximizing vertical displacement u_{out}^v . a) Deformed structure cut-out where $0.5 \leq \bar{\rho}_1$ and where $\bar{\rho}_2 = 0$ indicates electrode material and $\bar{\rho}_2 = 1$ EAP. Solid green lines indicates the undeformed configuration. b) Electric potential ϕ in the undeformed total domain with the design domain highlighted as a black square and outline of the final design in green. Note that the highest gradient is concentrated to the EAP material. c) Objective function with converged value $g_0 = -0.399$ mm at iteration 286. The designs for selected iterations are also shown. d) Volume constraints.

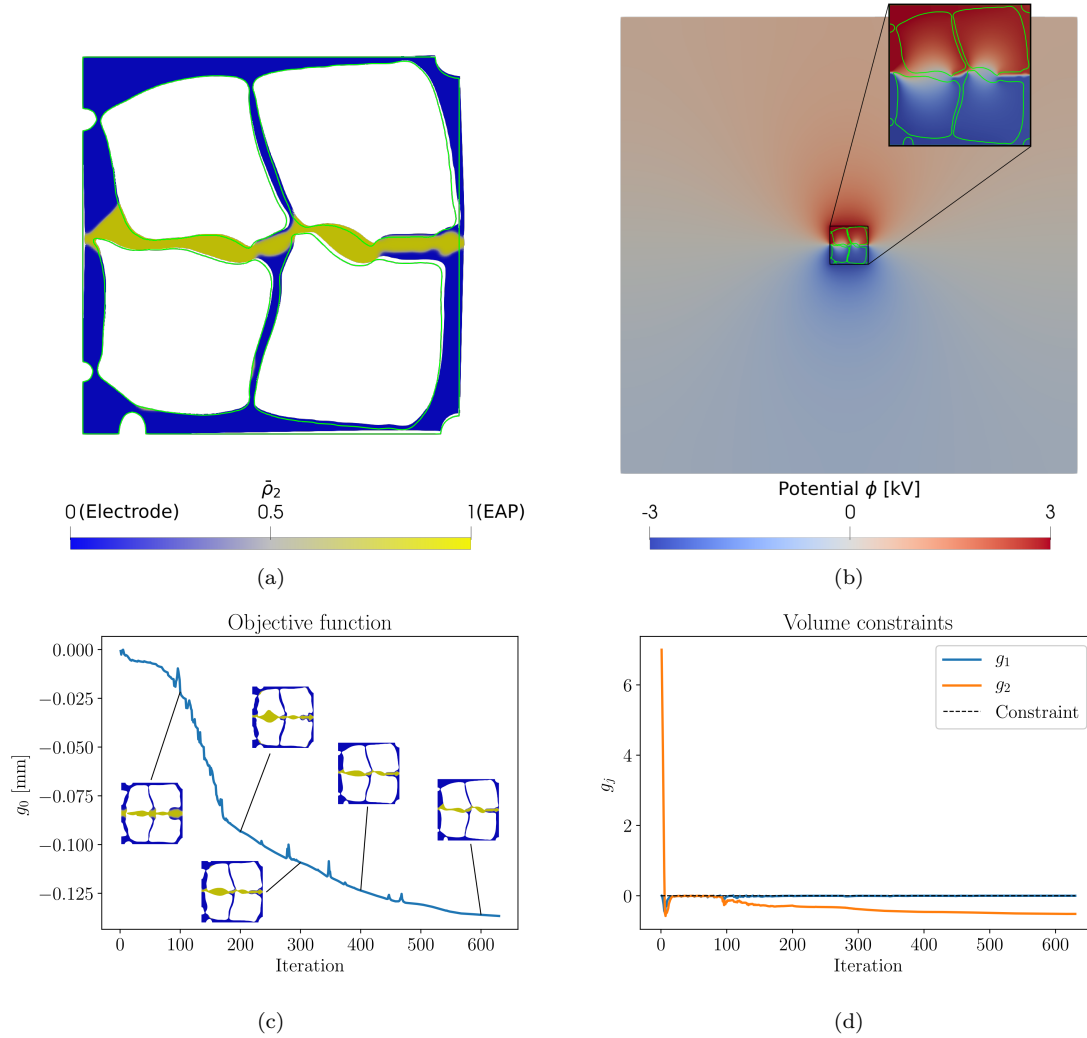


Figure 6: Optimized design for maximizing horizontal displacement u_{out}^h . a) Deformed structure cut-out where $0.5 \leq \bar{\rho}_1$ and where $\bar{\rho}_2 = 0$ indicates electrode material and $\bar{\rho}_2 = 1$ EAP. Solid green lines indicates the undeformed configuration. b) Electric potential ϕ in the undeformed total domain with the design domain highlighted as a black square and outline of the final design in green. Note that the highest gradient is concentrated to the EAP material. c) Objective function with converged value $g_0 = -0.137$ mm at iteration 630. The designs for selected iterations are also shown. d) Volume constraints.

5 Conclusions

This work presented a topology optimization methodology for generating EAP structures with arbitrary electrode and EAP layouts by utilizing density-based, multi-material topology optimization. Numerical test showed that common interpolation schemes were not able to create distinct material phases for the current problem. Due to this, an interpolation based on exponential functions, denoted exponential material interpolation, was introduced which allows for a large flexibility to control the material interpolation.

Standard regularization using the PDE filter and the smooth Heaviside projection was utilized on each density field. Despite the smooth Heaviside projection, the optimization might generate designs with intermediate densities. A recent work, see Thillaithevan et al. [34], suggested a penalization that were able to further decrease the amount of intermediate densities. This was successfully adopted in the current work by penalizing both density fields separately.

Most research on EAPs neglects the influence of the electric field in the free space surrounding a solid body. To model this influence, a truncated, extended domain method with vacuum permittivity and very low stiffness was used in this work. This is included in the governing equations for non-linear electro-elasticity by considering the computational domain as both the solid body and the free space with boundary conditions on the shared boundary.

The presented examples illustrates that this methodology is able to generate designs where the electrode and EAP material can take arbitrary layouts and still be connected to the electrical sources. Additionally, the generated designs consist of thin layers of EAP material with electrodes on each side, concentrating the electric field to the EAP material. This is similar to how traditional EAP structures are constructed, where a thin EAP layer is sandwiched between compliant electrodes.

Acknowledgements

The Swedish Research Council, Grants No. 2021-03851 and 2020-04364, is gratefully acknowledged for providing funding. Additionally, the authors would like to thank Krister Svanberg for his MMA implementation in Fortran.

Author contributions: CRediT

Daniel Hård: Conceptualization, Data curation, Formal Analysis, Investigation, Methodology, Software, Validation, Visualization, Writing – original draft, Writing – review & editing. **Mathias Wallin:** Funding acquisition, Supervision, Writing

– review & editing. **Matti Ristinmaa**: Funding acquisition, Supervision, Writing
– review & editing.

Funding data

This work was supported by the Swedish Research Council, Grants No. 2021-03851 and 2020-04364.

Conflict of interest

On behalf of all authors, the corresponding author states that there is no conflict of interest.

References

- [1] Bar-Cohen, Y., ed. *Electroactive polymer (EAP) actuators as artificial muscles: reality, potential, and challenges*. 2nd ed. Bellingham, Wash: SPIE Press, 2004. ISBN: 978-0-8194-5297-9.
- [2] Bar-Cohen, Y. and Anderson, I. A. “Electroactive polymer (EAP) actuators—background review”. en. In: *Mech Soft Mater* 1.1 (Mar. 2019), p. 5. ISSN: 2524-5619. DOI: 10.1007/s42558-019-0005-1.
- [3] Dorfmann, A. and Ogden, R. W. “Nonlinear electroelasticity”. en. In: *Acta Mechanica* 174.3 (Mar. 2005), pp. 167–183. ISSN: 1619-6937. DOI: 10.1007/s00707-004-0202-2.
- [4] Ask, A., Menzel, A., and Ristinmaa, M. “Phenomenological modeling of viscous electrostrictive polymers”. en. In: *International Journal of Non-Linear Mechanics*. Nonlinear Continuum Theories 47.2 (Mar. 2012), pp. 156–165. ISSN: 0020-7462. DOI: 10.1016/j.ijnonlinmec.2011.03.020.
- [5] Ask, A., Menzel, A., and Ristinmaa, M. “Electrostriction in electro-viscoelastic polymers”. en. In: *Mechanics of Materials* 50 (July 2012), pp. 9–21. ISSN: 0167-6636. DOI: 10.1016/j.mechmat.2012.01.009.
- [6] Ask, A., Menzel, A., and Ristinmaa, M. “Modelling of Viscoelastic Dielectric Elastomers with Deformation Dependent Electric Properties”. en. In: *Procedia IUTAM*. IUTAM Symposium on Mechanics of Soft Active Materials 12 (Jan. 2015), pp. 134–144. ISSN: 2210-9838. DOI: 10.1016/j.piutam.2014.12.015.

- [7] Ortigosa, R. and Gil, A. J. “A new framework for large strain electromechanics based on convex multi-variable strain energies: Finite Element discretisation and computational implementation”. In: *Computer Methods in Applied Mechanics and Engineering* 302 (Apr. 2016), pp. 329–360. ISSN: 0045-7825. DOI: 10.1016/j.cma.2015.12.007.
- [8] Bortot, E., Amir, O., and Shmuel, G. “Topology optimization of dielectric elastomers for wide tunable band gaps”. en. In: *International Journal of Solids and Structures* 143 (June 2018), pp. 262–273. ISSN: 0020-7683. DOI: 10.1016/j.ijsolstr.2018.03.014.
- [9] Sharma, A. K., Kosta, M., Shmuel, G., and Amir, O. “Gradient-based topology optimization of soft dielectrics as tunable phononic crystals”. en. In: *Composite Structures* 280 (Jan. 2022), p. 114846. ISSN: 0263-8223. DOI: 10.1016/j.compstruct.2021.114846.
- [10] Ortigosa, R., Martínez-Frutos, J., Ruiz, D., Donoso, A., and Bellido, J. C. “Density-based topology optimisation considering nonlinear electromechanics”. en. In: *Struct Multidisc Optim* 64.1 (July 2021), pp. 257–280. ISSN: 1615-1488. DOI: 10.1007/s00158-021-02886-3.
- [11] Ortigosa, R. and Martínez-Frutos, J. “Multi-resolution methods for the topology optimization of nonlinear electro-active polymers at large strains”. en. In: *Comput Mech* 68.2 (Aug. 2021), pp. 271–293. ISSN: 1432-0924. DOI: 10.1007/s00466-021-02030-4.
- [12] Martínez-Frutos, J., Ortigosa, R., and Gil, A. J. “In-silico design of electrode meso-architecture for shape morphing dielectric elastomers”. en. In: *Journal of the Mechanics and Physics of Solids* 157 (Dec. 2021), p. 104594. ISSN: 0022-5096. DOI: 10.1016/j.jmps.2021.104594.
- [13] Hård, D., Wallin, M., and Ristinmaa, M. “Connectivity Constraints Ensuring Continuous Electrodes in Topology Optimization of Electroactive Polymer”. In: *Journal of Mechanical Design* 146.101707 (Apr. 2024). ISSN: 1050-0472. DOI: 10.1115/1.4064980.
- [14] Bendsøe, M. P. and Sigmund, O. “Material interpolation schemes in topology optimization”. en. In: *Archive of Applied Mechanics* 69.9 (Nov. 1999), pp. 635–654. ISSN: 1432-0681. DOI: 10.1007/s004190050248.
- [15] Stegmann, J. and Lund, E. “Discrete material optimization of general composite shell structures”. en. In: *International Journal for Numerical Methods in Engineering* 62.14 (2005), pp. 2009–2027. ISSN: 1097-0207. DOI: 10.1002/nme.1259.

- [16] Yi, B., Yoon, G. H., Zheng, R., Liu, L., Li, D., and Peng, X. “A unified material interpolation for topology optimization of multi-materials”. In: *Computers & Structures* 282 (July 2023), p. 107041. ISSN: 0045-7949. DOI: 10.1016/j.compstruc.2023.107041.
- [17] Granlund, G., Wallin, M., Günther-Hanssen, O., Tortorelli, D., and Watts, S. “Topology optimization of compliant mechanisms under transient thermal conditions”. In: *Computer Methods in Applied Mechanics and Engineering* 418 (Jan. 2024), p. 116478. ISSN: 0045-7825. DOI: 10.1016/j.cma.2023.116478.
- [18] He, M., Zhang, X., Santos Fernandez, L. dos, Molter, A., Xia, L., and Shi, T. “Multi-material topology optimization of piezoelectric composite structures for energy harvesting”. In: *Composite Structures* 265 (June 2021), p. 113783. ISSN: 0263-8223. DOI: 10.1016/j.compstruct.2021.113783.
- [19] Hu, J., Wallin, M., Ristinmaa, M., Liu, Y., and Liu, S. “Integrated multi-material and multi-scale optimization of compliant structure with embedded movable piezoelectric actuators”. In: *Computer Methods in Applied Mechanics and Engineering* 421 (Mar. 2024), p. 116786. ISSN: 0045-7825. DOI: 10.1016/j.cma.2024.116786.
- [20] Almeida, B. V. de, Pavanello, R., and Langelaar, M. “Topology optimization of smart structures with embedded piezoelectric stack actuators using a composite geometry projection method”. In: *Computer Methods in Applied Mechanics and Engineering* 429 (Sept. 2024), p. 117120. ISSN: 0045-7825. DOI: 10.1016/j.cma.2024.117120.
- [21] Ortigosa, R., Martínez-Frutos, J., and Gil, A. J. “Programming shape-morphing electroactive polymers through multi-material topology optimisation”. en. In: *Applied Mathematical Modelling* 118 (June 2023), pp. 346–369. ISSN: 0307-904X. DOI: 10.1016/j.apm.2023.01.041.
- [22] Chen, Q. and Konrad, A. “A review of finite element open boundary techniques for static and quasi-static electromagnetic field problems”. In: *IEEE Transactions on Magnetics* 33.1 (Jan. 1997). Conference Name: IEEE Transactions on Magnetics, pp. 663–676. ISSN: 1941-0069. DOI: 10.1109/20.560095.
- [23] Vu, D. K. and Steinmann, P. “A 2-D coupled BEM–FEM simulation of electro-elastostatics at large strain”. In: *Computer Methods in Applied Mechanics and Engineering* 199.17 (Mar. 2010), pp. 1124–1133. ISSN: 0045-7825. DOI: 10.1016/j.cma.2009.12.001.

- [24] Vu, D. K. and Steinmann, P. “On 3-D coupled BEM–FEM simulation of nonlinear electro-elastostatics”. In: *Computer Methods in Applied Mechanics and Engineering* 201-204 (Jan. 2012), pp. 82–90. ISSN: 0045-7825. DOI: 10.1016/j.cma.2011.08.024.
- [25] Pelteret, J.-P., Davydov, D., McBride, A., Vu, D. K., and Steinmann, P. “Computational electro-elasticity and magneto-elasticity for quasi-incompressible media immersed in free space”. en. In: *International Journal for Numerical Methods in Engineering* 108.11 (2016), pp. 1307–1342. ISSN: 1097-0207. DOI: 10.1002/nme.5254.
- [26] Dev, C., Stankiewicz, G., and Steinmann, P. “On the influence of free space in topology optimization of electro-active polymers”. en. In: *Struct Multidisc Optim* 66.8 (Aug. 2023), p. 187. ISSN: 1615-1488. DOI: 10.1007/s00158-023-03634-5.
- [27] Jackson, J. D. *Classical electrodynamics*. eng. New York: Wiley, 1962. ISBN: 978-0-471-43131-2.
- [28] Eringen, A. C. and Maugin, G. A. *Electrodynamics of continua. 1: Foundations and solid media*. eng. New York Heidelberg: Springer, 1990. ISBN: 978-1-4612-7923-5 978-0-387-96936-7 978-3-540-96936-5.
- [29] Kovetz, A. *Electromagnetic theory*. Oxford science publications. Oxford ; New York: Oxford University Press, 2000. ISBN: 978-0-19-850604-1 978-0-19-850603-4.
- [30] Wang, F., Lazarov, B. S., Sigmund, O., and Jensen, J. S. “Interpolation scheme for fictitious domain techniques and topology optimization of finite strain elastic problems”. In: *Computer Methods in Applied Mechanics and Engineering* 276 (July 2014), pp. 453–472. ISSN: 0045-7825. DOI: 10.1016/j.cma.2014.03.021.
- [31] Lazarov, B. S. and Sigmund, O. “Filters in topology optimization based on Helmholtz-type differential equations”. en. In: *International Journal for Numerical Methods in Engineering* 86.6 (2011), pp. 765–781. ISSN: 1097-0207. DOI: 10.1002/nme.3072.
- [32] Wallin, M., Ivarsson, N., Amir, O., and Tortorelli, D. “Consistent boundary conditions for PDE filter regularization in topology optimization”. en. In: *Struct Multidisc Optim* 62.3 (Sept. 2020), pp. 1299–1311. ISSN: 1615-1488. DOI: 10.1007/s00158-020-02556-w.
- [33] Wang, F., Lazarov, B. S., and Sigmund, O. “On projection methods, convergence and robust formulations in topology optimization”. en. In: *Struct Multidisc Optim* 43.6 (June 2011), pp. 767–784. ISSN: 1615-1488. DOI: 10.1007/s00158-010-0602-y.

- [34] Thillaithevan, D., Murphy, R., Hewson, R., and Santer, M. “Inverse design of periodic microstructures with targeted nonlinear mechanical behaviour”. en. In: *Struct Multidisc Optim* 67.4 (Mar. 2024), p. 55. ISSN: 1615-1488. DOI: 10.1007/s00158-024-03761-7.
- [35] Granlund, G. and Wallin, M. “Large-scale elasto-plastic topology optimization”. en. In: *International Journal for Numerical Methods in Engineering* n/a.n/a (Aug. 2024), e7583. ISSN: 1097-0207. DOI: 10.1002/nme.7583.
- [36] Ye, H.-L., Wang, W.-W., Chen, N., and Sui, Y.-K. “Plate/shell topological optimization subjected to linear buckling constraints by adopting composite exponential filtering function”. en. In: *Acta Mech. Sin.* 32.4 (Aug. 2016), pp. 649–658. ISSN: 1614-3116. DOI: 10.1007/s10409-015-0531-5.
- [37] Svanberg, K. “The method of moving asymptotes—a new method for structural optimization”. en. In: *International Journal for Numerical Methods in Engineering* 24.2 (1987), pp. 359–373. ISSN: 1097-0207. DOI: 10.1002/nme.1620240207.